

See discussions, stats, and author profiles for this publication at: <https://www.researchgate.net/publication/327102980>

# Validation of the CFD-DPM solver DPMFoam in OpenFOAM® through analytical, numerical and experimental comparisons

Article in *Granular Matter* · November 2018

DOI: 10.1007/s10035-018-0834-x

CITATIONS

57

READS

3,292

4 authors:



Célio Fernandes

Faculty of Engineering at University of Porto (FEUP)

67 PUBLICATIONS 596 CITATIONS

SEE PROFILE



Denis Semyonov

Coolbrook Oy

4 PUBLICATIONS 73 CITATIONS

SEE PROFILE



L. L. Ferrás

University of Porto

124 PUBLICATIONS 1,000 CITATIONS

SEE PROFILE



J.M. Nobrega

University of Minho

215 PUBLICATIONS 2,195 CITATIONS

SEE PROFILE



# Validation of the CFD-DPM solver DPMFoam in OpenFOAM<sup>®</sup> through analytical, numerical and experimental comparisons

C. Fernandes<sup>1</sup> · D. Semyonov<sup>1</sup> · L. L. Ferrás<sup>1</sup> · J. Miguel Nóbrega<sup>1</sup>

Received: 23 January 2018  
© Springer-Verlag GmbH Germany, part of Springer Nature 2018

## Abstract

Multiphase flows are relevant in several industrial processes mainly because they are present in the production of a large diversity of products. Hence, the availability of accurate numerical modeling tools, able to cope with this type of flows, is of major significance to provide detailed information about the system characteristics, in order to guide the design activity. This study presents a detailed assessment of a multiphase flow solver able to couple Eulerian and Lagrangian phases, the last modeled through the discrete particle method. The numerical code is already implemented in the open source computational fluid dynamics software package OpenFOAM<sup>®</sup>. The solver (*DPMFoam*) is firstly used to simulate the collision between two particles, for which a good correlation was obtained with the theoretical impulse force value. Subsequently, the solver is employed in the simulation of a pseudo 2D gas-solid flow in a fluidized bed. In this case study, the results obtained for the bubble patterns, time-average flow patterns, bed expansion dynamics and particle phase energy analysis are in agreement with the experimental and numerical results available in the literature. In addition, the numerical pressure drop for the fluidized bed is computed and compared with the analytical Ergun's pressure drop equation. The accuracy of the numerical results was found to be sensitive to the solid fraction estimation.

**Keywords** Discrete particle method (DPM) · Particle flow · OpenFOAM<sup>®</sup> · Fluidized bed

## 1 Introduction

Multiphase flows are present in many processing technologies, lying from electrophotographic processes, to paper-making, to cavitating pumps and turbines, to the pellet form of practically all raw plastics. Consequently, the capability of predicting the flow behavior of a particle cloud is vital to maximize the productivity and success of those processes. Detailed information about the disperse and continuum phases can be obtained by using either experimental [1], theoretical [2–4] or numerical approaches [5–7]. All these studies can generally be categorized as Eulerian–Eulerian (separated) or Eulerian–Lagrangian (disperse) flows. Eulerian–Eulerian flows consist of a system of interpenetrating fluids/solids separated by no sharp interfaces. Eulerian–Lagrangian flows involve a finite number of

particles, drops or bubbles (disperse phase) spread in a continuous phase.

In the Eulerian–Eulerian models, both phases are governed by mass, momentum and energy conservation equations which include the interaction terms between the different phases. Hence, the Eulerian–Eulerian models neglect the discrete nature of the disperse phase. To characterize the properties of the material this approach uses averaging techniques [8,9] which involve major difficulties, related to the way the forces acting on the disperse phase are computed, the consideration of additional effects related to particle–particle and particle–fluid interactions and how to take into account the different mechanisms of inter-phase momentum and mass transfers. In addition, the boundary conditions required for the Eulerian–Eulerian models also present difficult modeling issues [10]. Generally, the Eulerian–Eulerian models are used to obtain macroscopic characteristics of the particulate process of interest. However, understanding the microscopic mechanism, based on the interactions between individual particles and interactions with surrounding fluids and walls, is fundamental to explore the interdisciplinary research on the discrete particle studies and to produce results which are

✉ C. Fernandes  
cbpf@dep.uminho.pt

<sup>1</sup> Institute for Polymers and Composites/i3N, University of Minho, Campus de Azurém, 4800-058 Guimarães, Portugal

physically meaningful [11]. In Eulerian–Lagrangian models, the disperse phase is studied by assessing either the motion of individual particles or the motion of particle agglomerates (parcels) [11]. The momentum transfer around each of the particles is computed by summing drag, lift and moment forces acting on those particles. One additional aspect which is taken into account in the Eulerian–Lagrangian models is the particle–particle interactions which happens in dense flows. A wide range of areas present this type of dense systems, namely, mining and milling operations, ploughing, fluidized beds, slurry pipelines, abrasive water jet machining, food processing, debris flows, avalanches, landslides, sediment transport and earthquake-induced soil liquefaction. When those interactions dominate the mechanics, the motions are called granular flows [12]. The rheology of granular flows will be strongly influenced by the dynamics of particle–particle interactions. Consequently, the dynamics of the particle–particle interactions must be established prior to a discussion of the rheology of the overall flow [13]. On rapid granular flows it is usually assumed instantaneous, binary, collisions between particles, the so-called hard particle model [6,14,15]. This assumption is valid for some applications, but it is now known that the high shear rates necessary to achieve such flow conditions are atypical [13]. More complex particle–particle interactions are present in most of the granular flows, where simultaneous particles collision can happen during the flow. The most often used model for this type of interactions found in computer simulations is the soft particle model [2,16,17]. In this model the inter-particle contact forces (normal damping and sliding forces) are computed using simple mechanical elements, such as springs, dash-pots and sliders. The trajectories of particles are calculated by the Newton’s second law. In addition, other non-contact forces can be incorporated into the soft particle model [4,18].

Difficulties arise when a Eulerian–Lagrangian simulation is made on an arbitrary 3D unstructured mesh, due to the availability of a tracking particle motion algorithm and the detection of the interaction between a particle and a complex geometry surface. Both problems have been solved in the open source OpenFOAM® framework [19], where the Lagrangian tracking is fully available [20] and the detection of particle–surface interaction using the soft-sphere discrete element model is also implemented by means of the RIGID algorithm [21]. OpenFOAM® is a C++ software based on object oriented programming [22], where the user can customize or extend the numerical libraries accordingly to their own needs. The Computational Fluid Dynamics and Discrete Element Method (CFD–DEM) which is implemented in the OpenFOAM® framework solves the locally averaged Navier–Stokes equation for the fluid flow by CFD which is continuum based, and Newton’s equation for the motion of the particle system by DEM which is discrete based [23]. The coupling between DEM and CFD computations is done

by exchanging fluid–particle interaction forces. However, the studies done until now to assess the accuracy of that solver are quite scarce [21].

In order to overcome the lack of results regarding the accuracy of the coupled CFD–DEM solver, *DPMFoam* [24], several studies are addressed in this work. In the next section, mathematical models for the continuous phase and soft-sphere discrete element phase are presented. The numerical method used to solve the coupled CFD–DEM system is described in Sect. 3. Numerical case studies to test the CFD–DEM solver are presented in Sect. 4. Firstly, the *DPMFoam* solver was used to study the contact between two particles and the results obtained were compared to the theoretical impulse force value. Secondly, the accuracy of the *DPMFoam* solver was also assessed, by simulating a pseudo 2D gas–solid flow in a fluidized bed. The numerical results obtained for the bubble patterns, time-average flow patterns, bed expansion dynamics and particle phase energy analysis were compared with numerical and experimental results provided by Goldschmidt [25]. The paper ends with the main conclusions.

## 2 Mathematical models

The so-called CFD–DEM approach is based on the Eulerian–Lagrangian scheme where the governing equations of the fluid–solid two-phase flow consist of the Navier–Stokes equations for the fluid flow and the discrete element method for particles motion. The motion of particles in the DEM is governed by the Newton’s laws of motion accordingly to the approach derived on Tsuji et al. [7,26] and the fluid in the CFD can be described by locally averaged Navier–Stokes equations [27].

Essential for the coupling between the Eulerian (fluid) and Lagrangian (particle) phases is the knowledge of the particle–fluid interaction forces. Common particle–fluid interaction forces include the buoyancy, pressure gradient, drag as well as other unsteady forces such as virtual mass, Basset and lift forces [4]. The formulation of the coupled CFD–DEM approach is described in Sects. 2.1 and 2.2.

### 2.1 Governing equations for the particle system

In the continuum approach the macroscopic behavior of particle flow is controlled by the interactions between individual particles as well as interactions with surrounding fluid and walls. Recognizing the microscopic mechanism in terms of these interactions is crucial to develop better strategies for process control. Such target is mostly achieved in terms of particle scale modeling. Discrete modeling can produce dynamic information, namely the trajectories of particles and transient forces acting on them, which is highly difficult, if not impossible, to obtain by physical experimentation.

Therefore, DEM has been progressively used in the past two decades or so.

A particle in a granular flow can have two types of motion: translational and rotational. During its movement, the particle may interact with its neighboring particles or walls and interact with the surrounding fluid, with which its momentum and energy are exchanged. Strictly speaking, particle movement is affected not only by the forces and torques produced from its immediate neighboring particles and fluid but also the particles and fluids more distant through the proliferation of disturbance waves. In DEM approach, it is commonly assumed that this problem can be taken into account by choosing a numerical time step less than a critical value. This way during a single time step the disturbance cannot multiply from the particle and fluid longer than its immediate neighboring particles and fluid [2]. Hence, at all times the resultant forces on a particle can be calculated entirely from its interaction with the contacting particles and fluid for coarse particle system. For a fine particle system, non-contact forces such as the electrostatic forces and van der Waals should also be considered. Based on these assumptions, Newton's second law of motion can be used to define the motion of individual particles. Following [2], the DEM is used to solve the governing equations for the motion of a particle  $i$  in the particle system:

$$m_i \frac{d\mathbf{U}_i^p}{dt} = \sum_{j=1}^{n_i^c} \mathbf{F}_{ij}^c + \sum_{k=1}^{n_i^{nc}} \mathbf{F}_{ik}^{nc} + \mathbf{F}_i^f + \mathbf{F}_i^g \quad (1)$$

$$I_i \frac{d\boldsymbol{\omega}_i}{dt} = \sum_{j=1}^{n_i^c} \mathbf{M}_{ij} \quad (2)$$

where  $\mathbf{U}_i^p$  and  $\boldsymbol{\omega}_i$  denote the translational and angular velocities of particle  $i$ , respectively,  $\mathbf{F}_{ij}^c$  and  $\mathbf{M}_{ij}$  are the contact force and contact torque acting on particle  $i$  by its  $j$  contact (either with a particle or a wall), respectively,  $\mathbf{F}_{ik}^{nc}$  is the non-contact force acting on particle  $i$  by particle  $k$  or other sources,  $n_i^c$  is the number of total contacts for particle  $i$ ,  $n_i^{nc}$  is the number of total non-contacts for particle  $i$ ,  $\mathbf{F}_i^f$  is the particle–fluid interaction force acting on particle  $i$ ,  $\mathbf{F}_i^g$  is the gravitational force and  $m_i$  and  $I_i$  are the mass and moment of inertia of particle  $i$ , respectively. Contact and non-contact forces between particles and particle–fluid interaction forces will be explained in Sects. 2.1.1 and 2.1.2.

For the gravitational force applied to spherical particles the following average density based formulation is adopted [3,28]:

$$\mathbf{F}_i^g = m_i \mathbf{g} = \frac{1}{6} \pi \rho_i d_i^3 \mathbf{g} \quad (3)$$

where  $m_i$ ,  $\rho_i$  and  $d_i$  are the mass, density and diameter of particle  $i$ , respectively, and  $\mathbf{g}$  is the gravity acceleration vector.

Figure 1 schematically shows the typical forces and torques involved in a DEM simulation. The inter-particle forces (tangential component,  $f_{ij}^t$ , and normal component,  $f_{ij}^n$ ) act at the contact point between particles rather than the mass centre of a particle and they will generate a torque,  $m_{ij}^r$ , causing the particle to rotate (rolling friction torque). The non-contact forces involve a combination of three fundamental forces, i.e. the van der Waals force (proportional to  $h^{-6}$ , where  $h$  is the separation distance between two spheres), capillary force (due to the surface tension at solid/liquid/gas interfaces, where  $\phi$  is the half-filling angle) and electrostatic force (due to charged particles), which can act concurrently or successively to different extents. The particle–fluid interaction force, mainly the drag force, is the driving force for fluidization, where  $\beta$  is the momentum exchange coefficient. Several models have been proposed to determine these forces and torques [4]. Once the forces and torques are known, Eqs. (1) and (2) can be solved numerically to obtain the trajectories and velocities of all particles involved in the system.

### 2.1.1 Particle–particle interaction forces

In general, the contact between two particles,  $\mathbf{F}_{ij}^c$ , is not at a single point but on a finite area due to the deformation of the particles, which would result in overlapping in the case of rigid bodies. The contact traction distribution over this area can be divided into a component in the contact plane (or tangential plane) and one normal to the plane. Hence, a contact force has two components: normal and tangential. In this work, each physical particle is mathematically defined by a sphere. The particles are allowed to overlap an amount of  $\Delta x$  and the normal,  $\mathbf{U}_n^p$ , and tangential,  $\mathbf{U}_t^p$ , relative velocities (at the contact point) determine the collision forces via a contact force law. Typically, linear models are the most natural and simple models, but more complex models can be used (see [29]). Figure 2 shows the simple spring-dashpot (may also be referred to as spring-slider-dashpot) model, proposed by Cundall and Strack [2], where the spring is used for the elastic deformation while the dashpot accounts for the viscous dissipation. The effects of these mechanical elements on particle motion appear through the following parameters: stiffness  $k$ , damping coefficient  $\eta$  and friction coefficient  $\mu$ . In this paper the Hertzian spring-dashpot model is used [26].

The normal component of the contact (particle–particle) force,  $\mathbf{F}_{nij}^c$ , when particle  $i$  is in contact with particle  $j$ , acting on particle  $i$  is given by the sum of the forces due to the spring and dash-pot

$$\mathbf{F}_{nij}^c = (-k_n |\delta_n| - \eta_n \mathbf{U}_{ij}^p \cdot \mathbf{n}) \mathbf{n} \quad (4)$$

and  $\mathbf{F}_{niw}^c$  for particle–wall contact is

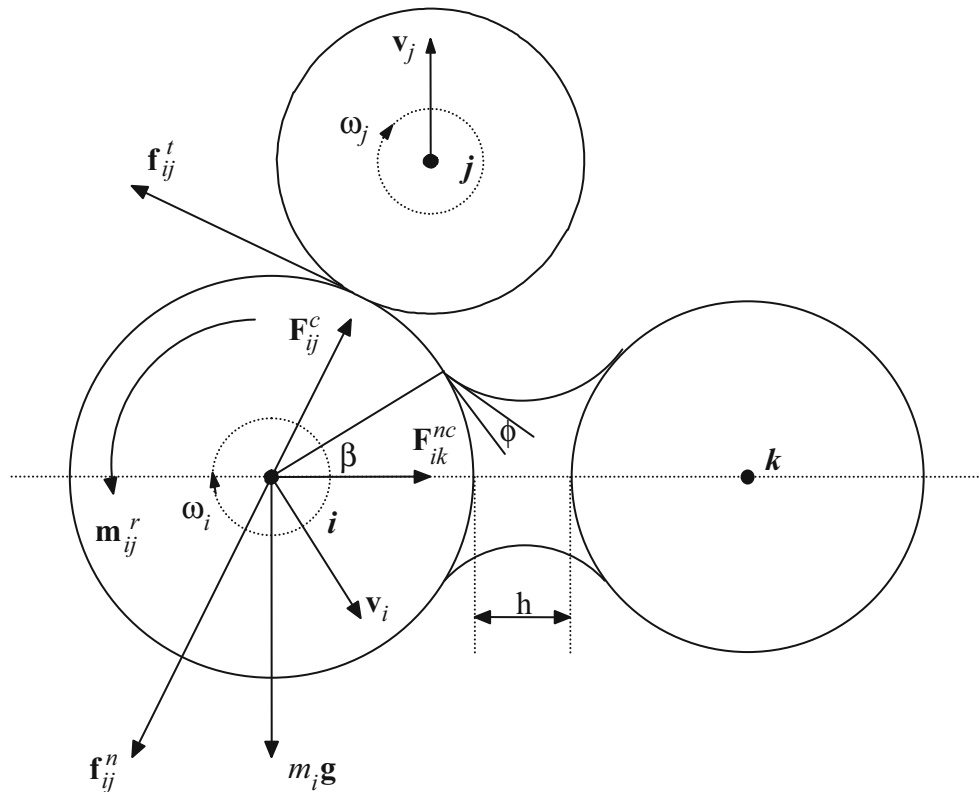


**Fig. 1** Schematic illustration of the forces acting on particle  $i$  from contacting particle  $j$  and non-contacting particle  $k$  (capillary force here)

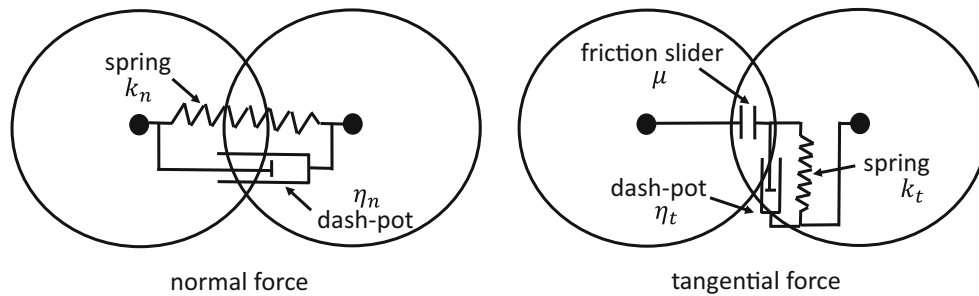


**Fig. 2** Schematic description of the spring-dashpot model

$$\mathbf{F}_{niw}^c = (-k_{nw}|\delta_{nw}| - \eta_{nw}\mathbf{U}_{iw}^p \cdot \mathbf{n}_w)\mathbf{n}_w \quad (5)$$

where  $k_n$  and  $\eta_n$  are the stiffness and the damping coefficients of particles in normal direction, respectively,  $k_{nw}$  and  $\eta_{nw}$  are those of walls, and,  $\delta_n$  and  $\delta_{nw}$  are the normal displacement for particle–particle and particle–wall interactions, respectively, whose magnitudes are given by

$$|\delta_n| = r_i + r_j - |\mathbf{p}_j - \mathbf{p}_i| \quad (6)$$

and

$$|\delta_{nw}| = r_i - |\mathbf{p}_i - \mathbf{p}_c| \quad (7)$$

where  $r_i$  and  $r_j$  are radii of particle  $i$  and  $j$ , respectively,  $\mathbf{p}_i$ ,  $\mathbf{p}_j$  and  $\mathbf{p}_c$  are the location vectors of particle  $i$ , particle  $j$  and contact point on the wall, respectively. For particle–particle interaction the velocity of particle  $i$  relative to particle  $j$ ,  $\mathbf{U}_{ij}^p$ , is given by

$$\mathbf{U}_{ij}^p = \mathbf{U}_i^p - \mathbf{U}_j^p \quad (8)$$

and for particle–wall interaction

$$\mathbf{U}_{iw}^p = \mathbf{U}_i^p - \mathbf{U}_w^p \quad (9)$$

where  $\mathbf{U}_i^p$  and  $\mathbf{U}_j^p$  are the translation velocities of particle  $i$  and particle  $j$ , respectively, and  $\mathbf{U}_w^p$  is the slip velocity of the sphere–wall contact point. In addition,  $\mathbf{n}$  and  $\mathbf{n}_w$  are the unit

vector pointing from the center of particle  $i$  to that of particle  $j$  and unit vector of the surface normal pointing outwards, respectively.

The tangential component of the contact (particle–particle) force,  $\mathbf{F}_{tij}^c$  is given by:

$$\mathbf{F}_{tij}^c = -k_t \delta_t - \eta_t \mathbf{U}_{tij}^p \quad (10)$$

and  $\mathbf{F}_{tiw}^c$  for particle–wall interaction

$$\mathbf{F}_{tiw}^c = -k_{tw} \delta_{tw} - \eta_{tw} \mathbf{U}_{tiw}^p \quad (11)$$

where  $k_t$  and  $\eta_t$  are the stiffness and the damping coefficients of particles in tangential direction, respectively,  $k_{tw}$  and  $\eta_{tw}$  are those of walls. The formulas for the tangential displacements  $\delta_t$  and  $\delta_{tw}$  for particle–particle and particle–wall contacts, respectively, can be found on Deen et al. [23]. The tangential slip velocity for particle–particle contact,  $\mathbf{U}_{tij}^p$ , is given by

$$\mathbf{U}_{tij}^p = \mathbf{U}_{ij}^p - (\mathbf{U}_{ij}^p \cdot \mathbf{n})\mathbf{n} + (r_i \boldsymbol{\omega}_i + r_j \boldsymbol{\omega}_j) \times \mathbf{n} \quad (12)$$

and for particle–wall contact,  $\mathbf{U}_{tiw}^p$ , is computed as

$$\mathbf{U}_{tiw}^p = \mathbf{U}_{iw}^p - (\mathbf{U}_{iw}^p \cdot \mathbf{n})\mathbf{n}_w + r_i \boldsymbol{\omega}_i \times \mathbf{n}_w \quad (13)$$

If the following relation is satisfied

$$|\mathbf{F}_{tij}^c| \geq \mu |\mathbf{F}_{nij}^c| \quad (14)$$

then particle  $i$  slides over particle  $j$  or wall and the tangential force can be written in the form of sliding friction force as

$$\mathbf{F}_{tij}^c = -\mu |\mathbf{F}_{nij}^c| \frac{\delta_t}{|\delta_t|} \quad (15)$$

where  $\mu$  is the friction coefficient. Equation (15) is the Coulomb-type friction law.

According to the Hertzian contact theory [30] the normal component of the contact force,  $\mathbf{F}_{nij}^c$ , varies with the 3/2 power of the displacement  $\delta_n$ . Hence, Eq. (4) is replaced by

$$\mathbf{F}_{nij}^c = (-K_n |\delta_n|^{3/2} - \eta_n \mathbf{U}_{ij}^p \cdot \mathbf{n})\mathbf{n} \quad (16)$$

where the stiffness coefficient,  $K_n$ , can be calculated by Hertzian contact theory when the physical properties such as Young's modulus and Poisson ratio are known (see [26]). Determination of other physical parameters, such as damping and friction coefficients can also be found in [26].

Finally, the total force acting on particle  $i$  is obtained by taking the summation of the above forces with respect to particle  $j$

$$\mathbf{F}_{ij}^c = \sum_{j=1}^{n_i^c} (\mathbf{F}_{nij}^c + \mathbf{F}_{tij}^c) \quad (17)$$

$$\mathbf{M}_{ij} = \sum_{j=1}^{n_i^c} (r_i \mathbf{n} \times \mathbf{F}_{tij}^c) \quad (18)$$

When fine particles are present and/or moisture exists, non-contact inter-particle forces,  $\mathbf{F}_{ik}^{nc}$ , may greatly affect the packing and flow behavior of particles. Usually the non-contact forces involve a compound of three fundamental forces, i.e. the capillary force, van der Waals force and electrostatic force, which can operate all together or separately to different extents. In this work, non-contact forces between particles are neglected.

### 2.1.2 Particle–fluid interaction forces

The surrounding fluid will have contact with particles, which will result in several particle–fluid interaction forces, in addition to the buoyancy force. Several of such forces have been implemented in DEM simulation, including particle–fluid drag, pressure gradient, and other unsteady forces such as virtual mass, Basset, and lift forces [3,4,31]. The particle–fluid interaction term,  $\mathbf{F}_i^f$ , that is used in Eq. (1) can be written as:

$$\mathbf{F}_i^f = \mathbf{F}_d + \mathbf{F}_{\nabla p} + \mathbf{F}_{\nabla \cdot \tau} + \mathbf{F}_{vm} + \mathbf{F}_B + \mathbf{F}_{Saff} + \mathbf{F}_{Mag} \quad (19)$$

where  $\mathbf{F}_d$  is the drag force,  $\mathbf{F}_{\nabla p}$  is the pressure gradient force,  $\mathbf{F}_{\nabla \cdot \tau}$  is the viscous force,  $\mathbf{F}_{vm}$  is the virtual mass force,  $\mathbf{F}_B$  is the Basset force and lift forces such as the Saffman force,  $\mathbf{F}_{Saff}$ , and the Magnus force,  $\mathbf{F}_{Mag}$ . In a gas-solid system, drag force and pressure gradient force are the only ones considered [4], where particle collisions and inter-particle forces are significant. Hence, in this work the fluid particle interaction force is calculated as:

$$\mathbf{F}_i^f = \mathbf{F}_d + \mathbf{F}_{\nabla p} \quad (20)$$

The drag force  $\mathbf{F}_d$  depends on the superficial velocity  $\mathbf{U}^s$ , which is proportional to the relative velocity between the phases. If  $\mathbf{U}^f$  and  $\mathbf{U}_i^p$  are the fluid and particle velocity respectively, then the superficial velocity is defined as:

$$\mathbf{U}^s = \epsilon_i (\mathbf{U}^f - \mathbf{U}_i^p) \quad (21)$$

where  $\epsilon_i$  is the particle porosity field given by

$$\epsilon_i = \frac{1}{V_{cell}} \sum_{\forall i \in cell} V_i \quad (22)$$



where  $V_i$  is the volume of particle  $i$  residing in the cell under consideration with volume  $V_{cell}$ . Equation (23) states the common equation for the drag force

$$\mathbf{F}_d = \frac{V_i \beta}{\epsilon_i} (\mathbf{U}^f - \mathbf{U}_i^p) \quad (23)$$

where  $\beta$  is the inter-phase momentum exchange coefficient. Many correlations have been proposed to compute the particle–fluid interaction drag force. In this work we adopt a commonly used drag-model, based on empirical correlations for bed pressure drop, which combines the drag relations by Ergun and Orning [32] and Wen and Yu [33]. For dense regimes ( $\epsilon_f < 0.8$ ), where  $\epsilon_f$  is the fluid porosity field satisfying  $\epsilon_f = 1 - \epsilon_i$ ,  $\beta$  is obtained from the well-known Ergun [32] equation

$$\beta = 150 \frac{\epsilon_i^2}{\epsilon_f} \frac{\mu_f}{d_i^2} + 1.75 \epsilon_i \frac{\rho_f}{d_i} |\mathbf{U}^f - \mathbf{U}_i^p| \quad (24)$$

and for more dilute regimes ( $\epsilon_f \geq 0.8$ ) the correlation proposed by Wen and Yu [33] is used

$$\beta = \frac{3}{4} C_d \frac{\epsilon_f \epsilon_i}{d_i} \rho_f |\mathbf{U}^f - \mathbf{U}_i^p| \epsilon_f^{-2.65} \quad (25)$$

where  $\mu_f$  and  $\rho_f$  are fluid dynamic viscosity and density, respectively, and  $d_i$  is the diameter of particle  $i$ . The drag coefficient  $C_d$  is a function of the particle Reynolds number,  $Re_p$ , given by

$$C_d = \begin{cases} \frac{24}{Re_p} (1 + 0.15 Re_p^{0.687}), & \text{if } Re_p \leq 1000 \\ 0.44, & \text{if } Re_p > 1000 \end{cases} \quad (26)$$

where  $Re_p = (\rho_f |\mathbf{U}^f - \mathbf{U}_i^p| d_i) / \mu_f$ .

The pressure gradient force,  $\mathbf{F}_{\nabla p}$ , is given as:

$$\mathbf{F}_{\nabla p} = -V_i \nabla p \quad (27)$$

## 2.2 Governing equations for fluid-phase flow

The motion of an incompressible fluid phase in the presence of a secondary particulate phase is governed by the volume-averaged continuity equation

$$\frac{\partial \epsilon_f}{\partial t} + \nabla \cdot (\epsilon_f \mathbf{U}^f) = 0 \quad (28)$$

and Navier-Stokes equations

$$\frac{\partial (\epsilon_f \mathbf{U}^f)}{\partial t} + \nabla \cdot (\epsilon_f \mathbf{U}^f \mathbf{U}^f) = -\nabla P - S_p + \nabla \cdot (\epsilon_f \boldsymbol{\tau}_f) + \epsilon_f \mathbf{g} \quad (29)$$

where  $P$  is the modified pressure ( $p/\rho_f$ ) and the fluid-phase viscous stress tensor  $\boldsymbol{\tau}_f$  is given by:

$$\boldsymbol{\tau}_f = \frac{1}{\rho_f} \left[ \left( \lambda_f + \frac{2}{3} \mu_f \right) (\nabla \cdot \mathbf{U}^f) \boldsymbol{\delta}_K + \mu_f \left( (\nabla \mathbf{U}^f) + (\nabla \mathbf{U}^f)^T \right) \right] \quad (30)$$

where  $\lambda_f$  is the fluid bulk viscosity and  $\boldsymbol{\delta}_K$  is the Kronecker delta. Under the present simulation condition, the fluid bulk viscosity  $\lambda_f$  can be neglected [34]. The two-way coupling between the fluid-phase and the particles is enforced via the source term  $S_p$  in the momentum equation, Eq. (29), of the fluid-phase. As the fluid drag and pressure gradient forces acting on each particle are known (see Sect. 2.1.2), according to Newton's third law of motion, the source term is computed as a volumetric fluid–particle interaction force given by:

$$S_p = \frac{\sum_{i=1}^{N_p} (\mathbf{F}_{d,i} + \mathbf{F}_{\nabla p,i})}{\rho_f V_{cell}} \quad (31)$$

where  $V_{cell}$  is the volume of a computational cell, and  $N_p$  is the number of particles located in this cell. It should be noted that to compute the fluid volume fraction  $\epsilon_f$  and volumetric fluid–particle interaction force  $S_p$  we need first to search for the cell in which the particle resides. For that, this work uses the particle tracking algorithm of Macpherson et al. [20], which is implemented for the unstructured, arbitrary polyhedral meshes available to use in the OpenFOAM® toolbox.

## 3 Numerical solution method

Since the governing equations in the DPM and CFD are different, the numerical solution of the mathematical models presented in Sect. 2 relies on different solution schemes.

The numerical solution of the translational and rotational motions, Eqs. (1) and (2), for the system composed by the discrete particles in the DPM approach, is based in the explicit time integration method (e.g. see [2,7,15]). The straightforward formulation and its low memory requirements are the main advantage of this method [27].

The numerical solution to solve the equations for the fluid phase, Eqs. (28) and (29), relies on the collocated Finite Volume Method (FVM) which uses the conservative integral forms of the governing equations for the Eulerian phase [35]. In this method the spatial derivatives over the computational cell volume are converted into integrals over their surfaces in terms of the flux, the time derivative is semi-discretized (i.e. approximated via Taylor series expansions), the grid points define the faces and the discretization reservoir points are at the center of the control volume, the fluxes are interpolated at each step and the integrals are evaluated by the use of the mean value theorem.

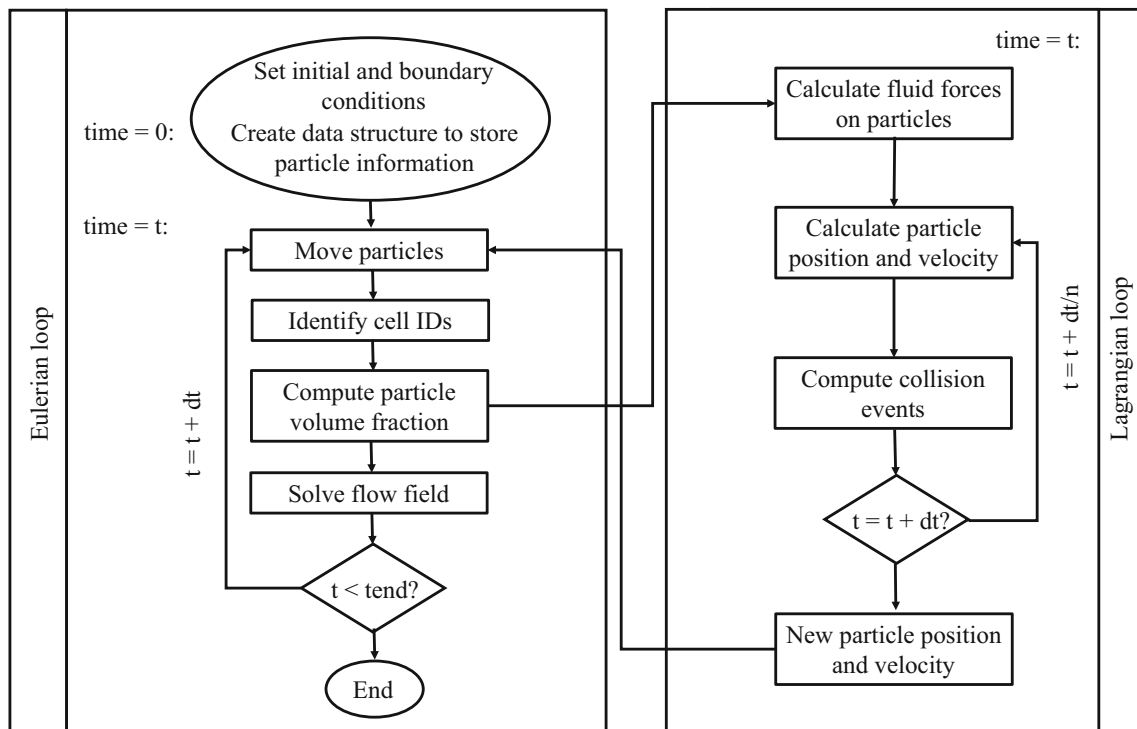


**Fig. 3** Flowchart of the Eulerian–Lagrangian algorithm

The implementation of the different equations involved is done using the OpenFOAM® C++ framework resources, which make possible the definition of variables directly as scalars, vectors or tensors [22].

The basis of the *DPMFoam* solver is the Lagrangian library source code (see [20,21]) coupled with the PIMPLE algorithm [36] used to solve the Eulerian phase. Initially, a CFD mesh with initial and boundary conditions for the Eulerian phase and a initial state for the Lagrangian phase are required. The main structure of the *DPMFoam* solver is illustrated in Fig. 3.

First, a data structure which contains all particle information is created. Then, the time loop starts and at the beginning of each time step the discrete-related (particle) operations are executed:

- The Lagrangian code calculates the particle positions and velocities.
- The particle positions and velocities are passed to the Eulerian code.
- Afterwards, the particles are located within the Eulerian mesh and, for each particle, the cell ID of the centre position is saved.
- The next step is to compute the particle volume fraction inside each cell.
- Based on the particle and fluid initial velocities and particle volume fraction, the fluid forces (drag, lift, etc.) acting

on each particle are calculated and particle–fluid momentum exchange terms are assembled from particle-based forces.

- The force information for each particle is communicated to the Lagrangian code and is used to compute the particle velocity field for the next time step.

On the Eulerian calculations the volume averaged continuity and Navier–Stokes equations are solved for the current time step using the PIMPLE algorithm, in which pressure and velocity are treated sequentially and obtained using a predictor–corrector procedure. The Eulerian solver calculates the fluid velocity taking into account the local particle volume fraction and momentum exchange. After discrete and continuous related operations are executed, the algorithm advances the time until end time specified by the user is achieved.

The Eulerian governing equations are discretized using second-order central difference scheme for the pressure gradient and divergence terms, second order linear upwind scheme for the advection term and a first-order Euler scheme for the time derivative. The resulting Eulerian linear discretized systems were solved by a Conjugate Gradient (CG) solver with Geometric Algebraic Multi-Grid (GAMG) preconditioning for pressure, which is faster than standard methods by solving first on coarser meshes, and a smooth-Solver with Gauss-Seidel smoothing for velocity, which is used only as a smoother to reduce residuals. As the solver is



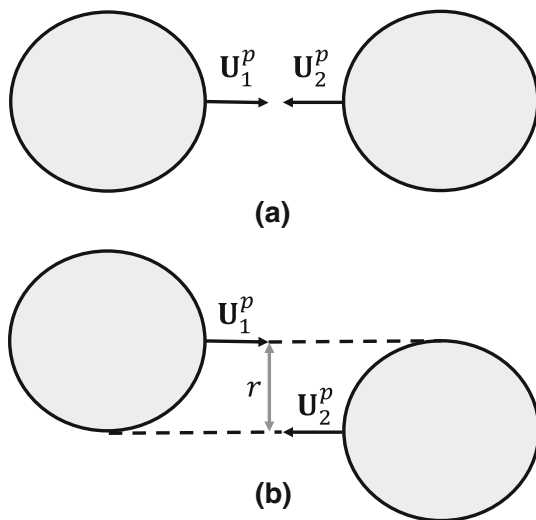


**Fig. 4** Particle–particle collision case studies configurations. **a** Normal collision. **b** Tangential collision

transient there is the need of convergence of all flow fields after each solving step, which was obtained using an absolute tolerance for pressure equal to  $10^{-6}$  and for velocity equal to  $10^{-5}$ . These values were established in preliminary trials, to verify which was the level required for convergence.

## 4 Test cases

In this section two case studies are presented in order to access the accuracy of the *DPMFoam* solver available in the OpenFOAM® framework. The first case study will focus on the collision between two particles. The numerical results obtained for the collision force are compared with the theoretical impulse force value. In the second study, the numerical simulation of a pseudo 2D gas-solid fluidized bed is performed. Numerical results obtained for the bubble patterns, time-average flow patterns, bed expansion dynamics and particle phase energy analysis are compared with the results obtained by Goldschmidt [25]. Finally, we present the comparison of the analytical Ergun pressure drop equation with the numerical pressure drop results obtained with *DPMFoam*.

### 4.1 Contact between two particles

In order to verify the spring-dashpot collision model, implemented in the OpenFOAM® framework Lagrangian library, two different collision events between two particles are studied: normal and tangential (see Fig. 4). The particles diameter and velocity are defined as 0.5 mm and 1 m/s, respectively.

A sensitivity analysis was performed to study the influence of some parameters, time-step ( $\Delta t$ ), collision resolution sub-steps (CRS), Young's modulus ( $E$ ) and cohesion energy

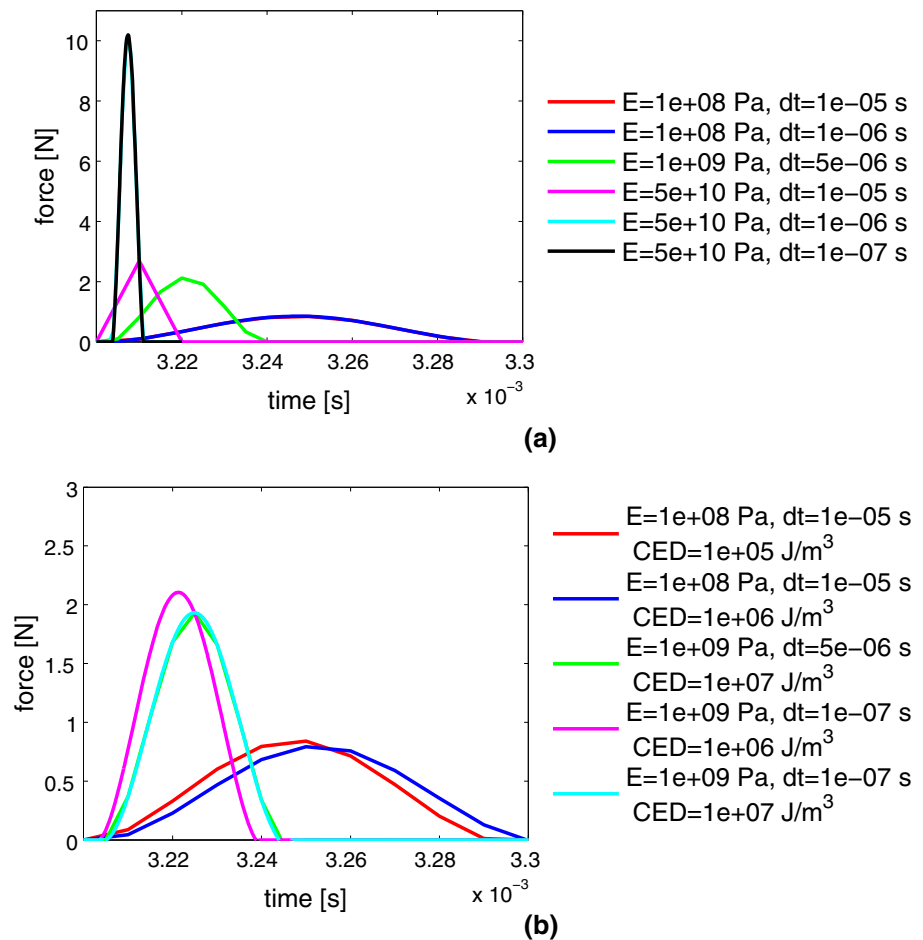
density (CED), on the contact force values predicted by the code, for the two configurations depicted in Fig. 4.

Figure 5 and Table 1 show the numerical results obtained for the force evolution along the two particles normal collision event. As can be seen from Fig. 5, for higher values of  $E$  shorter the collision time and, therefore, it requires smaller time-step to accurately resolve the collision. Another issue is that the CED parameter has a great importance in the accuracy of the computed interaction forces, even for a relatively large time-step (see Fig. 5b). In addition, Table 1 presents the maximum interpenetration value between the particles ( $\text{Interp}_{\max}$ , computed as the difference between the particle diameter and the minimum recorded distance between the particles), the estimated restitution coefficient ( $e_{\text{estimated}}$ , computed as the square root of the ratio between kinetic energy before and after collision, including linear and rotational parts), the collision time ( $t_{\text{collision}}$ , computed as the difference between the moments when collision ends and starts, which are obtained when the distance between two particles become less than the diameter - start - and then bigger than the diameter - end) and the numerical impulse force value ( $\text{Impulse}$ , computed as the integral of particle force values over collision time). The theoretical impulse force ( $\text{Impulse}_{\text{theo}} = F_{\text{average}} \Delta t = m \Delta v$ ) computed for this case is  $4.0758 \times 10^{-5}$  N.s. As can be seen in Table 1, cases 8–10, the numerical impulse force value is not accurately estimated for high values of  $E$  and large time steps. For all the other cases, the numerical impulse force is in the range of 2% of error from the theoretical value.

The numerical results obtained for the tangential collision event are shown in Table 2. For this case, the computed theoretical impulse force value is  $3.5298 \times 10^{-5}$  N.s. The cases with higher  $E$  (26–31) present an impulse force maximum error of 0.78% and on the cases with small values of  $E$  (Table 2 cases 32–35) the impulse force maximum error is 1.65%. This means that some differences exist on the numerical impulse force results when changing the  $E$  value, which are not present in the normal collision event where the differences are negligible. In addition, for lower  $E$  with no friction between particles (Table 2 cases 36–37), the numerical impulse force is within an error of 1.76% from the theoretical value. This means, as it was expected, that friction coefficient is also an important parameter in the collision event and, therefore, should be exactly defined to allow obtaining accurate results.

Summarizing, it can be stated that the spring-dashpot model implemented in the OpenFOAM® framework code was successfully assessed by comparing numerical collision data with theoretical values. The errors obtained for the two different collision events, using a sensitivity analysis by changing the time-step, the collision resolution sub-steps, the Young's modulus and the cohesion energy density param-

**Fig. 5** Particle–particle collision force evolution in the normal contact configuration. **a** No cohesion. **b** With cohesion



ters, are within 2% when compared to the theoretical impulse force value.

## 4.2 Gas-solid fluidized bed

In this case study the simulated system is a fluidized bed where both the gas phase hydrodynamics and the motion of all particles are resolved in a pseudo 2D geometry. To test the solver for dense particle flows, the experimental and numerical results of Goldschmidt [25] are chosen for comparison. The geometrical and flow conditions employed on Goldschmidt [25] are reproduced in our simulation. Figure 6 shows the geometry and mesh used in the simulations of the gas-solid fluidized bed, which consists of a rectangular container of dimension  $15 \times 150 \times 450$  mm (depth  $D \times$  width  $W \times$  height  $H$ ) with a grid of  $2 \times 30 \times 90$  cells. For the gas phase, side faces of the container are set to be walls with no-slip boundary conditions, front and back faces are set to symmetry, the outlet (top face) is set to a fixed value of zero for the pressure divided by density (Dirichlet boundary condition) and fixed velocity (Dirichlet boundary condition) for the inlet. For this last boundary condition, the velocity imposed, the so-called interstitial inlet velocity, is computed

based on the specified gas velocity value and the actual solid fraction at the boundary faces. Consequently, due to the non-constant solid fraction close to the boundary (result of the particles movement and eventual interpenetration on the inlet boundary), it gives a slightly different actual average velocity, which will keep the overall flow rate constant along time.

Parameters used in the CFD and DEM for the current case are listed in Table 3. For the discrete phase (Lagrangian phase) a bed with  $N_p = 24750$  glass beads was placed in the container. Initial particle distribution was set to be close to the one used by Goldschmidt in his thesis [25]. Initially the bed has height  $H_b = 150$  mm and solid fraction, given by the ratio between particles and bed volumes,  $\epsilon_i = V_p/V_b = \frac{N_p \times \pi/6 \times d_p^3}{W \times D \times H_b} \approx 0.6$ . Several values of the gas inflow velocity were used in the simulations. They were ranged from 0.1 to 2.0 times the theoretical minimum fluidization velocity. Absolute values were ranged from 0.125 to 2.5 m/s. Following [25] procedure, whose results correspond to an average of 5 s, the numerical flow statistics were obtained by averaging a period of 5 s of the total simulation time (10–20 s), using a fixed time-step of  $2 \times 10^{-5}$  s (which corresponds to a maximum Courant number of approximately 0.2).

**Table 1** Quantitative comparison of normal collision event

#	dt (s)	CED (J/m <sup>3</sup> )	E (Pa)	CRS	Interp <sub>max</sub> (m)	$e_{estimated}$	$t_{collision}$ (s)	Impulse (N·s)
1	1e−05	0	1e+08	12	5.817e−05	0.97102	9e−05	4.0479e−05
2	1e−05	0	1e+08	100	5.815e−05	0.97235	9e−05	4.0456e−05
3	1e−05	0	1e+08	1000	5.817e−05	0.97102	9e−05	4.0479e−05
4	1e−06	0	1e+08	12	5.841e−05	0.97224	8.8e−05	4.0479e−05
5	1e−06	0	1e+08	100	5.841e−05	0.97225	8.8e−05	4.0481e−05
6	1e−06	0	1e+08	1000	5.842e−05	0.97229	8.8e−05	4.0481e−05
7	5e−06	0	1e+09	20	2.31e−05	0.96963	3.5e−05	4.0486e−05
8	1e−05	0	5e+10	12	2.064e−06	0.97283	1e−05	2.6832e−05
9	1e−05	0	5e+10	100	2.086e−06	0.97228	1e−05	2.725e−05
10	1e−05	0	5e+10	1000	2.087e−06	0.97229	1e−05	2.727e−05
11	1e−06	0	5e+10	12	4.781e−06	0.97158	8e−06	4.0375e−05
12	1e−06	0	5e+10	100	4.778e−06	0.97229	8e−06	4.0352e−05
13	1e−06	0	5e+10	1000	4.778e−06	0.97229	8e−06	4.0351e−05
14	1e−07	0	5e+10	12	4.863e−06	0.97234	7.3e−06	4.0481e−05
15	1e−07	0	5e+10	100	4.864e−06	0.97230	7.3e−06	4.0484e−05
16	1e−07	0	5e+10	1000	4.864e−06	0.97229	7.3e−06	4.0483e−05
17	1e−05	1e+05	1e+08	12	5.906e−05	0.97093	9e−05	4.0487e−05
18	1e−05	1e+06	1e+08	12	6.735e−05	0.96637	1e−04	4.036e−05
19	1e−05	1e+05	1e+08	100	5.903e−05	0.97183	9e−05	4.0464e−05
20	1e−05	1e+06	1e+08	100	6.729e−05	0.96612	1e−04	4.0319e−05
21	1e−06	1e+05	1e+08	100	5.903e−05	0.97174	9e−05	4.0462e−05
22	1e−06	1e+06	1e+08	100	6.729e−05	0.96602	1e−04	4.0317e−05
23	5e−06	1e+07	1e+09	20	2.983e−05	0.95598	4.5e−05	4.0066e−05
24	1e−07	1e+06	1e+09	20	2.374e−05	0.96911	3.57e−05	4.0414e−05
25	1e−07	1e+07	1e+09	20	2.983e−05	0.95744	4.3e−05	4.0175e−05

**Table 2** Quantitative comparison of tangential collision event

#	dt (s)	CED (J/m <sup>3</sup> )	E (Pa)	CRS	Interp <sub>max</sub> (m)	$e_{estimated}$	$t_{collision}$ (s)	Impulse (N·s)
26	1e−06	0	5e + 10	12	4.317e−06	0.97298	7e−06	3.5028e−05
27	1e−06	0	5e + 10	100	4.316e−06	0.97248	7e−06	3.5023e−05
28	1e−06	0	5e + 10	1000	4.316e−06	0.97245	7e−06	3.5023e−05
29	1e−07	0	5e + 10	12	4.333e−06	0.97240	7.5e−06	3.503e−05
30	1e−07	0	5e + 10	100	4.333e−06	0.97235	7.5e−06	3.503e−05
31	1e−07	0	5e + 10	1000	4.333e−06	0.97237	7.5e−06	3.5031e−05
32	1e−05	0	1e + 08	12	5.13e−05	0.97229	9e−05	3.4715e−05
33	1e−06	0	1e + 08	12	5.179e−05	0.97348	9e−05	3.4721e−05
34	1e−06	0	1e + 08	100	5.179e−05	0.97343	9e−05	3.4717e−05
35	1e−06	0	1e + 08	1000	5.179e−05	0.97335	9e−05	3.4714e−05
<i>No friction between particles (<math>\mu = 0</math>)</i>								
36	1e−05	0	1e + 08	12	5.128e−05	0.96936	9e−05	3.4678e−05
37	1e−07	0	1e + 08	1000	5.177e−05	0.97212	9.01e−05	3.4679e−05

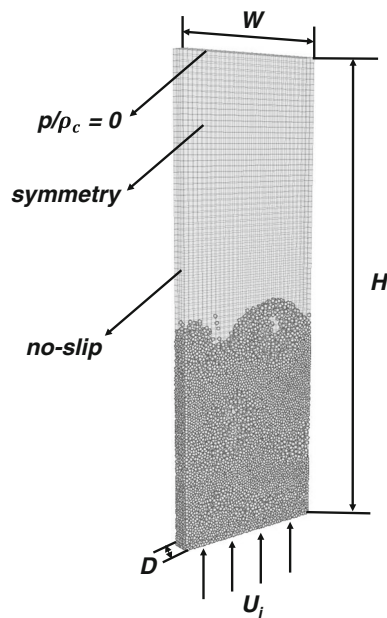


**Fig. 6** Geometry and mesh representation of the simulated pseudo 2D gas-fluidized bed

The following sections show the comparison between the numerical results obtained by the *DPMFoam* solver and Goldschmidt results [25]. The results obtained correspond to inflow superficial velocities of 1.25, 1.5 and 2.0 times the minimum fluidization velocity. As the minimum fluidization velocity considered on Goldschmidt [25] was 1.25 m/s, then the real gas velocities imposed in the simulations were 1.5625, 1.875 and 2.5 m/s. The Goldschmidt [25] results used for comparison in this study were obtained from numer-

ical simulations (using the two-fluid model, TFM, and the DPM hard-sphere model) and experimental measurements.

#### 4.2.1 Comparison of bubble patterns

Figure 7 shows images taken from the experiments and simulations (hard-sphere and TFM models) performed by Goldschmidt [25] comparing with *DPMFoam* results at the initial phase of the particle movement ( $t = 2.76$  s for  $1.25 U_{mf}$ ,  $t = 4.61$  s for  $1.5 U_{mf}$  and  $t = 0.59$  s for  $2.0 U_{mf}$ ). As can be concluded *DPMFoam* can predict slugging fluidization, since the *DPMFoam* results compares well with the experimental and the other two numerical models. The *DPMFoam* solver can predict larger bubbles when compared to the ones obtained by other methods (see white space on the left graphics of Fig. 7) as the fluidization velocity increases. The results obtained for the three simulated cases show that the discrete particle simulations (*DPMFoam* and DPM with hard-sphere model) produce the best agreement between numerical simulations and experimental results. In addition, the *DPMFoam* is capable to capture initialization of small bubbles near the bottom of the bed and strings of particles within larger bubbles like they are observed in experiments.

#### 4.2.2 Comparison of time-average flow patterns

More than being able to catch the bubble pattern, the CFD models should allow to predict the correct time-average bed behavior. The time-average solid fraction, which is obtained from averaging the measured particle volume fractions, is presented in Fig. 8. The experimental results in Fig. 8 show that the highest values of the particle fractions occur near

**Table 3** Parameters used in the simulation of the pseudo 2D fluidized bed.

Variables	Values
Simulation geometry:	
Width, $W$	150 mm
Depth, $D$	15 mm
Height, $H$	450 mm
Particle properties (DEM) [37]:	
Particle density, $\rho_p$	2526 kg/m <sup>3</sup>
Particle diameter, $d_p$	2.5 mm
Coefficient of normal restitution for particle–particle/wall, $e_n/e_{n,w}$	0.97/0.97
Coefficient of friction for particle–particle/wall, $\mu/\mu_w$	0.10/0.09
Poisson's ratio, $\nu$	0.35
Young's modulus, $E$	$1 \times 10^8$ Pa
Inlet gas velocity, $U_i$	0.125–2.5 m/s
Fluid properties (CFD):	
Gas density, $\rho_c$	1.2 kg/m <sup>3</sup>
Dynamic viscosity of gas, $\mu_c$	$1.2 \times 10^{-5}$ Pa·s

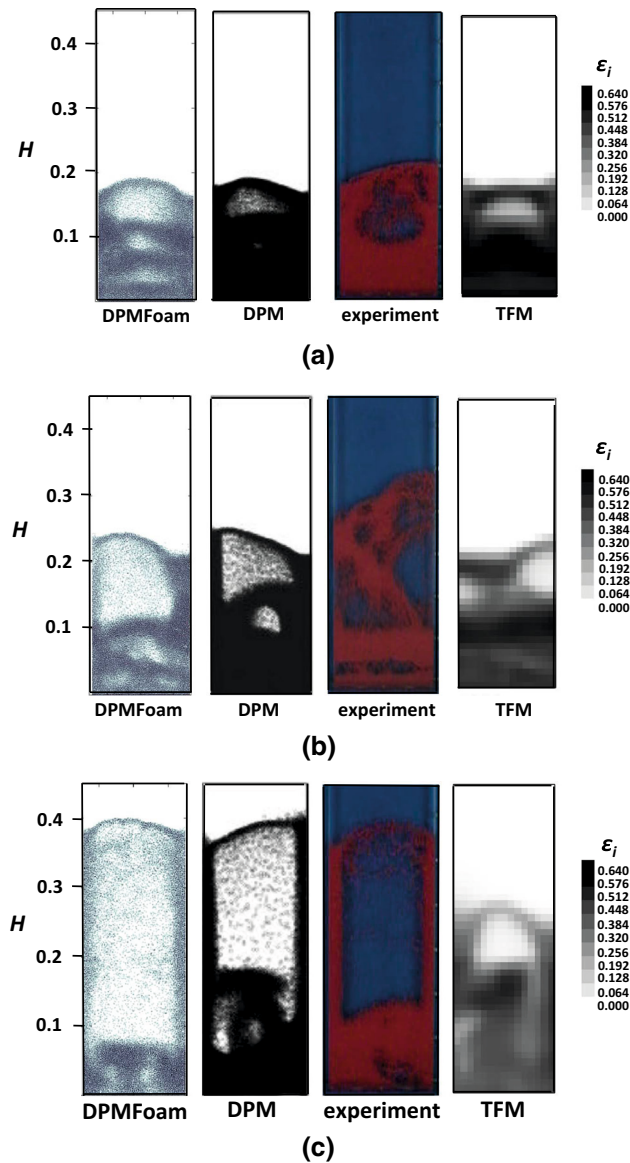


**Fig. 7** Snapshots of the bubble eruption for different inflow velocities. Left to right: *DPMFoam*, Goldschmidt DPM [25], Goldschmidt experiments [25], Goldschmidt Two-Fluid Model [25] ( $\epsilon_i$  is the solid fraction). **a**  $1.25 U_{mf}$ . **b**  $1.5 U_{mf}$ . **c**  $2.0 U_{mf}$

the geometry walls for higher fluidization velocities. The reason of this behavior is that bubbles mostly pass through the center of the bed, and at the moment of eruption particles are expelled into the walls. In the case of the discrete particle models used, it can be concluded that the time-average particle volume fraction profiles are very similar to the experimental results (higher volume fractions near the walls), while the TFM profiles are more homogeneous. This fact is due to the absence of small bubbles near the bottom of the bed, and the rise of bubbles along the lateral walls and through the core of the bed in the TFM. Finally, is worth to mention that from Fig. 8 we can conclude that for  $1.25 U_{mf}$

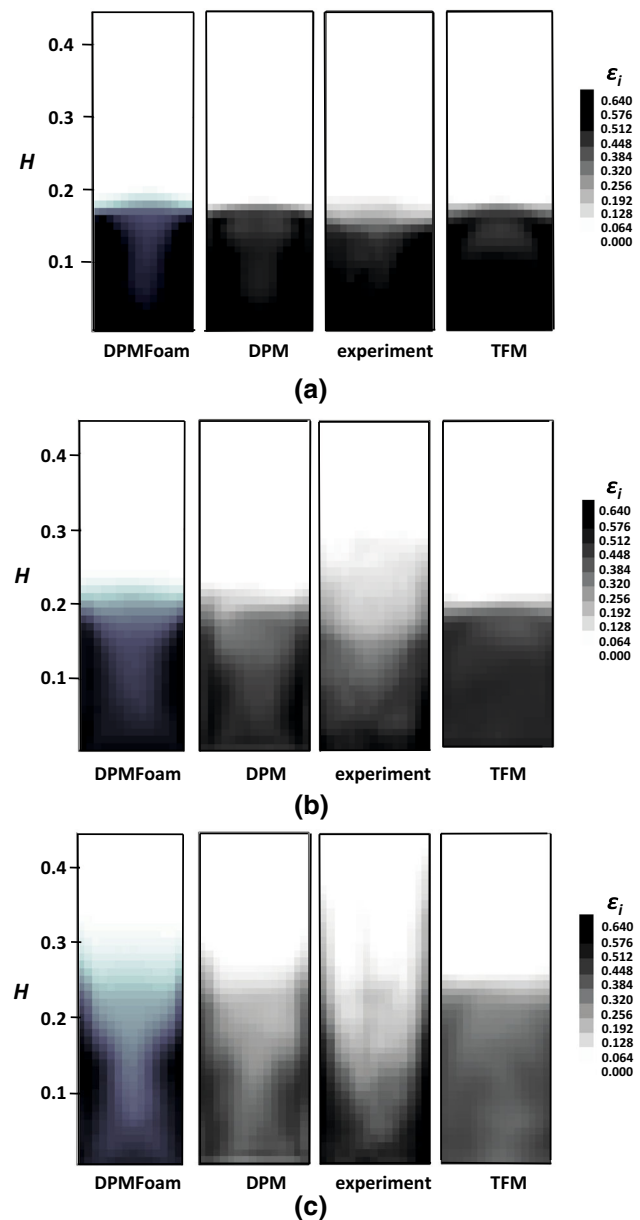


**Fig. 8** Comparison of measured time average ( $t = 5-10$  s) particle volume fractions to results of CFD simulations for different inflow velocities. Left to right: *DPMFoam*, Goldschmidt DPM [25], Goldschmidt experiment [25], Goldschmidt Two-Fluid Model [25] ( $\epsilon_i$  is the solid fraction). **a**  $1.25 U_{mf}$ . **b**  $1.5 U_{mf}$ . **c**  $2.0 U_{mf}$

and  $1.5 U_{mf}$  the experimental bed expansion is somewhat higher than all the results predicted by the numerical simulations, as it will be confirmed by the measurements presented in Sect. 4.2.3.

In addition the volume fraction weighted averaging of the particle phase velocity field for all models are compared in Fig. 9. In the case of the discrete particle models the particle phase velocity for each cell is computed from averaging the velocities of all particles inside that cell. Figure 9 shows that, except for  $1.25 U_{mf}$ , all models present similar time-average



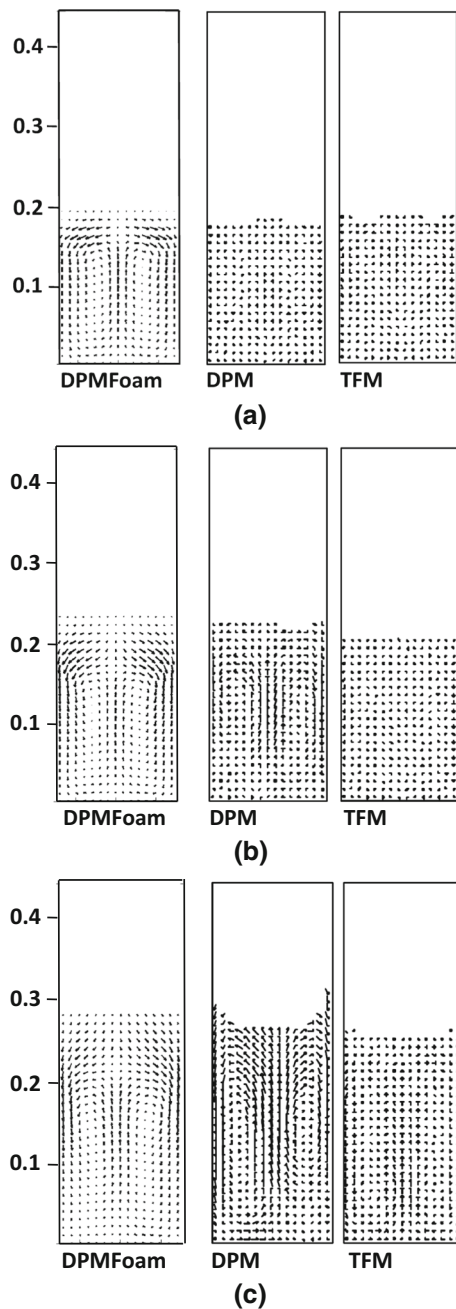


**Fig. 9** Comparison between time-average ( $t = 5\text{--}10$  s) particle velocities for different inflow velocities. Left to right: *DPMFoam*, Goldschmidt DPM [25], Goldschmidt Two-Fluid Model [25]. **a**  $1.25 U_{mf}$ . **b**  $1.5 U_{mf}$ . **c**  $2.0 U_{mf}$

particle flow profiles, i.e., upward flow through the center of the column and downward flow near the geometry walls. Furthermore, it can be seen that the discrete particle models show stronger flow pattern than the one obtained with the two-fluid model.

The comparisons made until this point are merely based on snapshots obtained from the results computed by *DPMFoam* and the ones provided by Goldschmidt [25], but a more

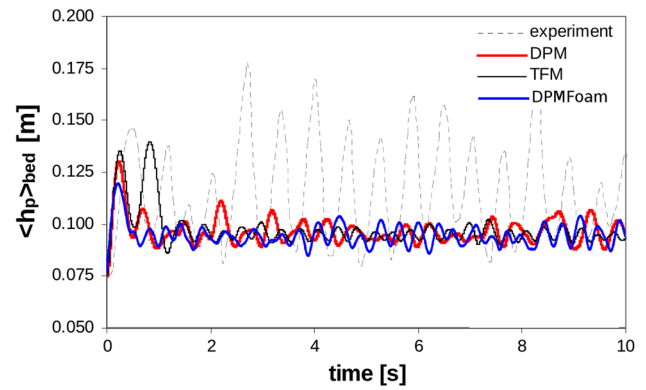


**Fig. 10** Comparison of measured and simulated average particle heights at  $1.5 U_{mf}$

comprehensive data analysis is presented on the next two sections.

#### 4.2.3 Comparison of bed expansion dynamics

*DPMFoam* was also evaluated in terms of the prediction of the bed expansion dynamics by doing the average of particle bed height,  $\langle h_p \rangle_{bed}$ . The formula used for this purpose is given by:

$$\langle h_p \rangle_{bed} = \frac{\sum_i^{N_{part}} h_i}{N_{part}} \quad (32)$$

where  $N_{part}$  is the total number of particles in the fluidized bed and  $h_i$  is the height of each one of those particles. Figure 10 is an example of the bed expansion dynamics for the  $1.5 U_{mf}$  case. The *DPMFoam* solver can predict higher bed expansion as the fluidization velocity increases and it under-predicts the particle bed height up to a time of 4 s when compared to Goldschmidt DPM model [25]. The time-average particle bed height ( $\langle h_p \rangle_t$ ), the intensity of the particle bed height fluctuations ( $RMS\langle h_p \rangle$ ) and the dominant fluctuation frequency were computed for the *DPMFoam* simulations and compared against Goldschmidt DPM model, TFM model and experiments, as presented in Table 4. As can be seen in Table 4 the average particle bed height over time obtained by *DPMFoam* is similar to the DPM and TFM models and, the particle bed height fluctuations (RMS) obtained by *DPMFoam* is similar to the DPM model, but in both cases the numerical results under-predict the experimental ones. Moreover, the frequency of the particle bed height fluctuations is higher in the numerical results than in the experiments, however, the predictions provided by *DPMFoam*, DPM and TFM models show the same trend.



**Table 4** Overview of experimental and simulated bed expansion dynamics

	Fluidization velocity	$\langle h_p \rangle_t$ (m)	$RMS \langle h_p \rangle$ (m)	Expansion freq. (Hz)
Experiment	1.25 $U_{mf}$	0.092	0.0098	1.6
DPM		0.085	0.0016	3.2
<i>DPMFoam</i>		0.083	0.0021	2.9
TFM		0.085	0.0020	3.0
Experiment	1.50 $U_{mf}$	0.114	0.0226	1.6
DPM		0.097	0.0052	2.0
<i>DPMFoam</i>		0.094	0.0044	2.6
TFM		0.095	0.0026	2.8
Experiment	2.00 $U_{mf}$	0.135	0.0323	1.4
DPM		0.120	0.0074	2.0
<i>DPMFoam</i>		0.116	0.0084	2.1
TFM		0.118	0.0039	2.4

#### 4.2.4 Comparison of particle phase energy analysis of CFD models

Energy balance for the bed was also calculated and compared with the Goldschmidt data [25]. Potential ( $E_{pot}$ ), kinetic ( $E_{kin}$ ) and rotational ( $E_{rot}$ ) energy were computed. According to Goldschmidt [25], kinetic energy can also be split in two components: kinetic energy due to convective movement of particles,  $E_{conv}$ , and granular energy due to random movement of the particles,  $E_{gran}$ . Hence, the total amount of energy of the particles in the system is given by:

$$E_{tot} = E_{pot} + E_{conv} + E_{gran} + E_{rot} \quad (33)$$

where

$$E_{pot} = \sum_i^{N_{part}} m_i g h_i \quad (34)$$

$$E_{kin} = \sum_i^{N_{part}} \frac{1}{2} m_i v_i^2 \quad (35)$$

$$E_{conv} = \sum_k^{N_{cell}} N_{part,k} \frac{1}{2} m_p < v_p >_k^2 \quad (36)$$

$$E_{gran} = \sum_k^{N_{cell}} N_{part,k} \frac{3}{2} m_p \theta_k \quad (37)$$

$$E_{rot} = \sum_i^{N_{part}} \frac{1}{2} I \omega_i^2 \quad (38)$$

In these equations,  $m$  and  $I$  are the mass and moment of inertia of a single particle, respectively,  $v$  and  $\omega$  are the particle's instantaneous translation and rotational velocity, respectively,  $h$  is the height of the particle,  $g$  is the gravity acceleration vector,  $< v_p >_k$  is the cell-averaged particle's

velocity,  $N_{part}$  is the number of particles in the system,  $N_{cell}$  is the number of mesh cells,  $N_{part,k}$  is the number of particles in cell  $k$  and  $\theta$  is the granular temperature [25] in the cell which is computed as:

$$\theta = \frac{1}{3} \frac{\sum_i^{N_{part,k}} (v_i - < v_p >_k)^2}{N_{part,k}} \quad (39)$$

Figure 11 show the time evolution of the energy analysis for the discrete particle simulation at  $1.5U_{mf}$ . As can be seen the energy levels continuously change as a result of dissipation and forces acting on the particles. It can be concluded from Fig. 11 that both discrete models, Goldschmidt DPM and *DPMFoam*, predict that most energy is present as potential energy and the amount of rotational energy is negligible. To compare these results for the different numerical models and imposed conditions they were time-averaged over the last 5 s of the simulation. Table 5 summarizes the absolute energy levels and relative contribution of all energy terms in all simulated models. It can be concluded that the total energy accumulation predicted by the three models at all operating conditions is about the same, being the errors less than 5%. However it can be seen in Table 5 that the total energy accumulation from the DPM solver is higher than the one obtained with *DPMFoam*, while the results from the TFM solver are lower at higher velocities than the ones given by *DPMFoam*. Again, the results presented in Table 5 clearly show that almost all energy is present as potential energy and the amount of rotational energy is negligible at all simulated conditions. Moreover, the energy resultant of granular motion is much higher in the *DPMFoam* simulations than in the Goldschmidt DPM and TFM simulations, which can be explained by the use of the soft-sphere contact model, that theoretically allows the simultaneous contact between multiple particles, thus increasing the granular temperature on the

**Fig. 11** Time dependency of bed energies for the discrete particle models. **a** Goldschmidt's DPM energy results. **b** *DPMFoam* energy results. **c** Closeup to granular and rotational energies of *DPMFoam* results

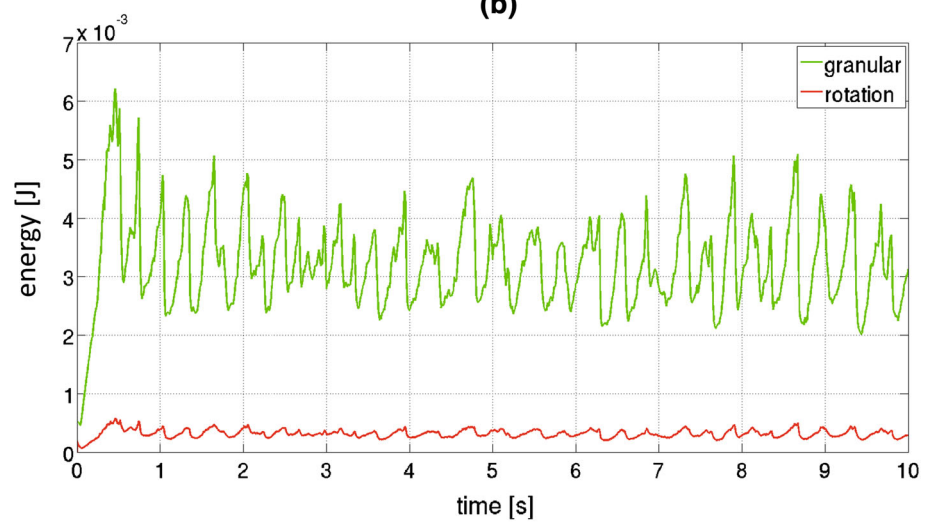
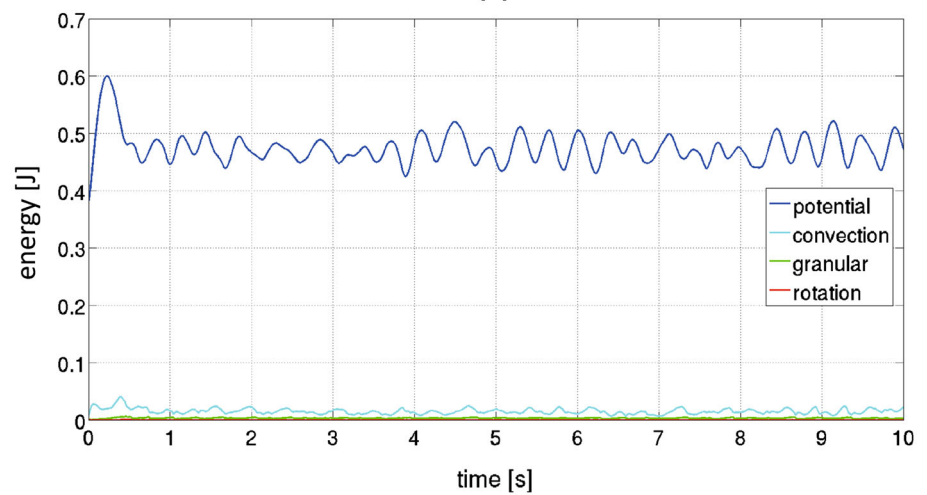
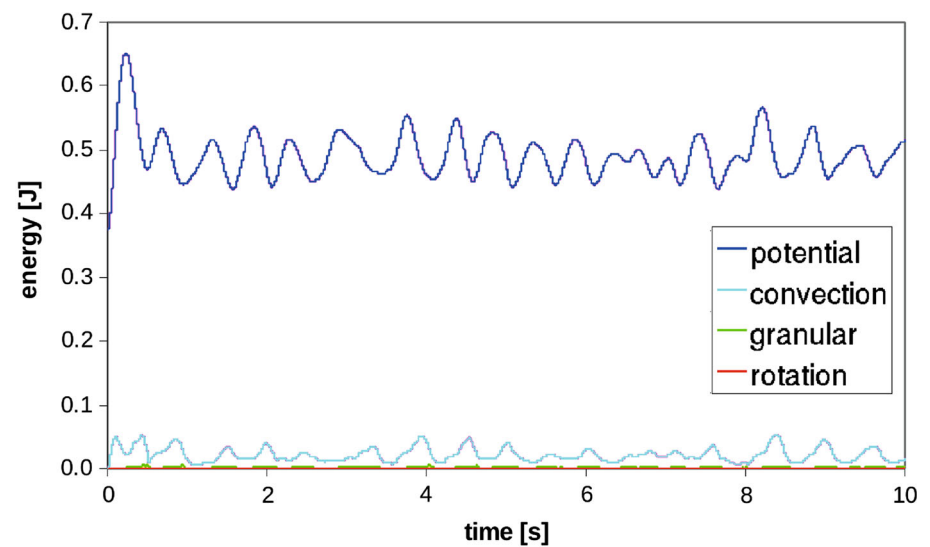


**Table 5** Quantitative comparison of energy data

	Fluidization velocity	$E_{tot}$ (J)	$\frac{E_{pot}}{E_{tot}}$ (%)	$\frac{E_{gran}}{E_{tot}}$ (%)	$\frac{E_{conv}}{E_{tot}}$ (%)	$\frac{E_{rot}}{E_{tot}}$ (%)
DPM	1.25 $U_{mf}$	0.431	99	0.13	0.85	0.02
<i>DPMFoam</i>		0.426	98.2	0.40	1.36	0.04
TFM		0.430	99	0.28	0.72	–
DPM	1.50 $U_{mf}$	0.507	96	0.32	3.64	0.04
<i>DPMFoam</i>		0.493	96.3	0.56	3.08	0.06
TFM		0.484	98	0.5	1.5	–
DPM	2.00 $U_{mf}$	0.660	91	0.63	8.28	0.09
<i>DPMFoam</i>		0.627	92.6	0.93	6.37	0.1
TFM		0.619	95	0.85	4.15	–

system [see Eq. (39)] and consequently the granular energy component. Additionally, the particle phase convection was much stronger in the discrete particle simulations (see Fig. 9).

#### 4.2.5 Ergun pressure drop

Suppose that a fluid is passed upwards through a bed of particles, then the pressure loss in the fluid due to frictional resistance increases with increasing fluid flow. There will be a moment where the upward drag force exerted by the fluid on the particles is equal to the apparent weight of particles in the bed. At this point, the bed becomes fluidized due to the fact that particles are lifted by the fluid, and the separation between particles increase. According to fluidization theory [38] the maximum theoretical pressure drop can be written as follows:

$$\Delta p_{theor,max} = \langle h_p \rangle_t (1 - \epsilon_i) (\rho_p - \rho_f) g \quad (40)$$

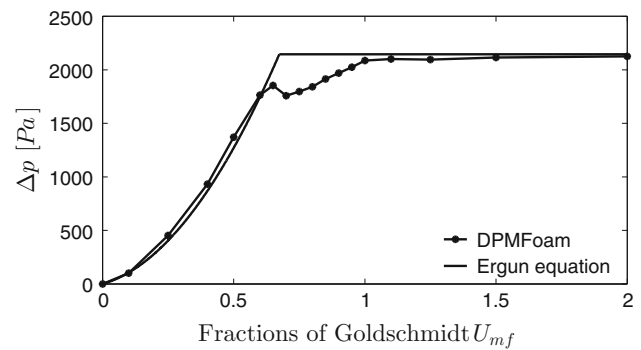
where  $\rho_p$  is the particle density,  $\rho_f$  is the fluid density,  $\langle h_p \rangle_t$  is the time average bed height,  $\epsilon_i$  is the particle volume fraction (in this work equal to 0.31331, the mean value of the time average particle volume fractions corresponding to each inlet fluidized velocity) and  $g$  is the gravity acceleration vector. The analytic formula to compute the pressure drop for a under-fluidized bed, at any flow conditions, was given on Ergun and Orning [32] as:

$$\frac{\Delta p}{\langle h_p \rangle_t} = 150 \frac{(1 - \epsilon_i)^2}{\epsilon_i^3} \frac{\mu U}{d^2} + 1.75 \frac{(1 - \epsilon_i)}{\epsilon_i^3} \frac{\rho_f U^2}{d} \quad (41)$$

where  $\mu$  is the fluid dynamic viscosity,  $U$  is the superficial fluid velocity through the bed and  $d$  is the particle diameter.

Comparison of the pressure drop numerical results, obtained by the *DPMFoam* solver, with the analytic formula given by Ergun and Orning [32], Eq. (41), is shown in Fig. 12.

In general, the results obtained show that *DPMFoam* correctly predicts the pressure drop when compared with the

**Fig. 12** Pressure drop through the bed

analytic formula. Due to the soft sphere model used, which allows a certain sphere interpenetration, the solid fraction is not constant even before the fluidization starts. This leads that after some point the solid fraction starts to slightly decrease with the increase of the superficial velocity, yielding numerical fluidization in the range of 0.65–1  $U_{mf}$ . As can be seen in Fig. 12, near the minimum fluidization velocity, *DPMFoam* behave differently when compared to the analytic curve. At this point, the numerical predictions are under-estimated, but with the increase of velocity it approaches the maximum theoretical value [given by Eq. (40)]. The estimated value of the minimum fluidization velocity is very sensitive to estimate of the solid fraction values. This means that the accuracy of the estimated pressure drop strongly depends on the accuracy of the estimated solid fraction value.

## 5 Conclusions

This work describes the numerical validation of a multiphase flow solver able to couple Eulerian and Lagrangian phases using the soft-sphere discrete particle method. The numerical code for dense granular flows is available in the open-source software OpenFOAM® and can significantly increase the potential of DEM simulations on industrial applications. The

solver, *DPMFoam*, is tested in two case studies, including collision between two particles and a pseudo 2D gas-solid fluidized bed. The following conclusions were reached for each case study.

Our numerical results for the normal collision event between two particles show that the numerical impulse force is in the range of 2% of error from the theoretical impulse force, except for cases where higher Young's modulus value is used simultaneously with a higher time-step. In the tangential collision event between two particles, the results showed that both for higher and lower Young's modulus value the numerical impulse force is in the range of 0.78% and 1.65% of error from the theoretical impulse force, respectively. In addition, if no friction between particles is considered for the case with lower Young's modulus, the error increased to 1.76%.

In the pseudo 2D fluidized bed case study, the results obtained are in good agreement with the numerical results of Goldschmidt [25] and follows the same trend of their experimental results, when bubble patterns, time-average flow patterns, bed expansion dynamics and particle phase energy analysis are compared. The numerical prediction of the pressure drop in the fluidized bed is found to be in good agreement to the analytical Ergun pressure drop equation, except near the minimum fluidization velocity zone which is sensitive to the solid fraction estimation.

**Acknowledgements** This work is funded by FEDER funds through the COMPETE 2020 Programme and National Funds through FCT Portuguese Foundation for Science and Technology under the project EXPL/CTM-POL/1299/2013. In addition, the authors would like to acknowledge the Minho University cluster under the project Search-ON2: Revitalization of HPC infrastructure of Minho, (NORTE-07-0162-FEDER-000086), co-funded by the North Portugal Regional Operational Programme (ON.2-0 Novo Norte), under the National Strategic Reference Framework (NSRF), through the European Regional Development Fund (ERDF).

## Compliance with ethical standards

**Conflict of interest** The authors declare that they have no conflict of interest.

## References

- Weighardt, K.: Experiments in granular flow. *Ann. Rev. Fluid Mech.* **7**, 89–114 (1975). <https://doi.org/10.1146/annurev.fl.07.010175.000513>
- Cundall, P.A., Strack, O.: A discrete numerical model for granular assemblies. *Géotechnique* **29**(1), 47–65 (1979). <https://doi.org/10.1680/geot.1979.29.1.47>
- O'Sullivan, C.: *Particulate Discrete Element Modelling: A Geomechanics Perspective*. Spon Press (an imprint of Taylor & Francis), London (2011)
- Zhu, H.P., Zhou, Z.Y., Yang, R.Y., Yu, A.B.: Discrete particle simulation of particulate systems: theoretical developments. *Chem. Eng. Sci.* **62**(13), 3378–3396 (2007). <https://doi.org/10.1016/j.ces.2006.12.089>
- Hoomans, B.P.B.: Granular dynamics of gas-solid two-phase flow. PhD thesis, University of Twente (2000)
- Campbell, C.S., Brennen, C.E.: Computer simulation of granular shear flows. *J. Fluid Mech.* **151**, 167–188 (1985a). <https://doi.org/10.1017/S002211208500091X>
- Tsuji, Y., Kawaguchi, T., Tanaka, T.: Discrete particle simulation of two-dimensional fluidized bed. *Powder Technol.* **77**(1), 79–87 (1993). [https://doi.org/10.1016/0032-5910\(93\)85010-7](https://doi.org/10.1016/0032-5910(93)85010-7)
- Gidaspow, D., Seo, Y.C., Ettehadieh, B.: Hydrodynamics of fluidization-experimental and theoretical bubble sizes in a two-dimensional bed with a jet. *Chem. Eng. Commun.* **22**, 253–272 (1983). <https://doi.org/10.1080/00986448308940060>
- Pfleger, D., Gomes, S., Gilbert, N., Wagner, H.G.: Hydrodynamic simulations of laboratory scale bubble columns fundamental studies of the Eulerian–Eulerian modelling approach. *Chem. Eng. Sci.* **54**, 5091–5099 (1999). [https://doi.org/10.1016/S0009-2509\(99\)00261-4](https://doi.org/10.1016/S0009-2509(99)00261-4)
- Morel, C.: *Mathematical Modeling of Disperse Two-Phase Flows*. Springer International Publishing, Switzerland (2015)
- Jakobsen, H.A., Sannaes, B.H., Grevskott, S., Svendsen, H.F.: Modeling of vertical bubble-driven flows. *Ind. Eng. Chem. Res.* **36**, 4052–4074 (1997). [https://doi.org/10.1016/0021-9991\(86\)90099-9](https://doi.org/10.1016/0021-9991(86)90099-9)
- Brennen, C.E.: *Fundamentals of Multiphase Flows*. Cambridge University Press, California (2005)
- Campbell, C.S.: Granular shear flows at the elastic limit. *J. Fluid Mech.* **465**, 261–291 (2002). <https://doi.org/10.1002/9781444304275.ch6>
- Campbell, C.S., Brennen, C.E.: Chute flows of granular material: some computer simulation. *ASME J. Appl. Mech.* **52**(1), 172–178 (1985b). <https://doi.org/10.1115/1.3168990>
- Hoomans, B.P.B., Kuipers, J.A.M., Briels, W.J., vanSwaaij, W.P.M.: Discrete particle simulation of bubble and slug formation in a two-dimensional gas-fluidised bed: a hard-sphere approach. *Chem. Eng. Sci.* **51**, 99–118 (1996). [https://doi.org/10.1016/0009-2509\(95\)00271-5](https://doi.org/10.1016/0009-2509(95)00271-5)
- Walton, O.R., Braun, R.L.: Viscosity, granular-temperature, and stress calculations for shearing assemblies of inelastic, frictional disks. *J. Rheol.* **30**, 949–980 (1986a). <https://doi.org/10.1122/1.549893>
- Walton, O.R., Braun, R.L.: Stress calculations for assemblies of inelastic spheres in uniform shear. *Acta Mech.* **63**, 73–86 (1986b). <https://doi.org/10.1007/BF01182541>
- Zhu, H.P., Zhou, Z.Y., Yang, R.Y., Yu, A.B.: Discrete particle simulation of particulate systems: a review of major applications and findings. *Chem. Eng. Sci.* **63**, 5728–5770 (2008). <https://doi.org/10.1016/j.ces.2008.08.006>
- OpenFOAM: The open source computational fluid dynamics toolbox (2011). [www.openfoam.com](http://www.openfoam.com)
- Macpherson, G.B., Nordin, N., Weller, H.G.: Particle tracking in unstructured, arbitrary polyhedral meshes for use in CFD and molecular dynamics. *Commun. Numer. Methods Eng.* **25**, 263–273 (2009). <https://doi.org/10.1002/cnm.1128>
- Su, J., Gu, Z., Xu, X.Y.: Discrete element simulation of particle flow in arbitrarily complex geometries. *Chem. Eng. Sci.* **66**, 6069–6088 (2011). <https://doi.org/10.1016/j.ces.2011.08.025>
- Weller, H.G., Tabor, G., Jasak, H., Fureby, C.: A tensorial approach to computational continuum mechanics using object-oriented techniques. *Comput. Phys.* **12**, 620–631 (1998). <https://doi.org/10.1146/annurev.fl.07.010175.000513>
- Deen, N.G., Van Sint Annaland, M., Van der Hoef, M.A., Kuipers, J.A.M.: Review of discrete particle modeling of fluidized beds. *Chem. Eng. Sci.* **62**, 28–44 (2007). <https://doi.org/10.1016/j.ces.2006.08.014>

24. OpenFOAM 2.3.0: Discrete particle modelling (2014). <http://openfoam.org/release/2-3-0/dpm/>
25. Goldschmidt, M.: Hydrodynamic Modelling of Fluidised Bed Spray Granulation. PhD thesis, University of Twente (2001)
26. Tsuji, Y., Tanaka, T., Ishida, T.: Lagrangian numerical simulation of plug flow of cohesionless particles in a horizontal pipe. *Powder Technol.* **71**(3), 239–250 (1992). [https://doi.org/10.1016/0032-5910\(92\)88030-L](https://doi.org/10.1016/0032-5910(92)88030-L)
27. Xu, B.H., Yu, A.B.: Numerical simulation of the gas-solid flow in a fluidized bed by combining discrete particle method with computational fluid dynamics. *Chem. Eng. Sci.* **52**, 2785–2809 (1997). [https://doi.org/10.1016/S0009-2509\(97\)00081-X](https://doi.org/10.1016/S0009-2509(97)00081-X)
28. Kafui, K.D., Thornton, C., Adams, M.J.: Discrete particle-continuum fluid modelling of gas-solid fluidised beds. *Chem. Eng. Sci.* **57**(13), 2395–2410 (2002). [https://doi.org/10.1016/S0009-2509\(02\)00140-9](https://doi.org/10.1016/S0009-2509(02)00140-9)
29. Schäfer, J., Dippel, S., Wolf, D.E.: Force schemes in simulation of granular material. *J. de Phys. I France* **6**(1), 5–20 (1996). <https://doi.org/10.1051/jp1:1996129>
30. Hertz, H.: Über die berührung fester elastischer körper (on the contact of elastic solids.). *J. Reine und Angew. Math.* **92**, 156–171 (1882)
31. Xiong, Y.Q., Zhang, M.Y., Yuan, Z.L.: Three-dimensional numerical simulation method for gas-solid injector. *Powder Technol.* **160**(3), 180–189 (2005). <https://doi.org/10.1016/j.powtec.2005.08.029>
32. Ergun, S., Orning, A.: Fluid flow through randomly packed columns and fluidized beds. *Ind. Eng. Chem.* **41**(6), 1179–1184 (1949). <https://doi.org/10.1021/ie50474a011>
33. Wen, C., Yu, Y.: Mechanics of fluidization. In: *Chemical Engineering Process Symposium*, pp. 100–111 (1966)
34. Bird, R.B., Stewart, W.E., Lightfoot, E.N.: *Transport Phenomena*. Wiley, New York (1960)
35. Ferziger, J.H., Peric, M.: *Computational Methods for Fluid Dynamics*. Springer, Berlin (2001)
36. Issa, R.I.: Solution of the implicitly discretized fluid flow equations by operator-splitting. *J. Comput. Phys.* **62**, 40–65 (1986). [https://doi.org/10.1016/0021-9991\(86\)90099-9](https://doi.org/10.1016/0021-9991(86)90099-9)
37. Gorham, D.A., Kharaz, A.H.: Results of particle impact tests. Technical report, Impact Research Group IRG 13, The Open University, Milton Keynes, UK (1999)
38. Rhodes, M.: *Introduction to Particle Technology*. Wiley, New York (2008)